Nanoscale

Multimetallic post-synthetic modifications of copper selenide nanoparticles

Journal:	*Nanoscale*
Manuscript ID	NR-ART-01-2023-000441.R1
Article Type:	Paper
Date Submitted by the Author:	24-Feb-2023
Complete List of Authors:	Sen, Riti; University of Pittsburgh, Chemistry Gordon, Tyler; University of Pittsburgh, Chemistry Millheim, Shelby; University of Pittsburgh, Chemistry Smith, Jacob; University of Pittsburgh, Chemistry Gan, Xing Yee; University of Texas Millstone, Jill; University of Pittsburgh, Chemistry

ARTICLE

Multimetallic post-synthetic modifications of copper selenide nanoparticles

Riti Sen[a], Tyler Masato Gordon[a], Shelby Liz Millheim[a], Jacob Harrison Smith[a], Xing Yee Gan[b], Jill Erin Millstone*[a^+]

Received 00th January 20xx,
Accepted 00th January 20xx

DOI: 10.1039/x0xx00000x

In this report, we investigate the addition of two metal cations, simultaneously and sequentially to $Cu_{2-x}Se$ nanoparticles. The metal combinations (Ag-Au, Ag-Pt, Hg-Au and Hg-Pt) are chosen such that one metal adds to the structure via cation exchange and the other adds to the structure via metal deposition when added individually to $Cu_{2-x}Se$ nanoparticles. Surprisingly, we find that for each metal combination, across all three synthesis routes, cation exchange and metal deposition products are obtained without deviation from the outcomes seen in the binary metal systems. However, within those outcomes the data show several types of heterogeneities in the morphologies formed including extent and composition of cation exchange products as well as the extent and composition of the metal deposited products. Taken together, these results suggest a hierarchical control for nanoheterostructure morphologies where the pathways of cation exchange or metal deposition in post-synthetic modification of $Cu_{2-x}Se$ exhibit relatively general outcomes as a function of metal, regardless of synthetic approach or metal combination. However, the detailed composition and interface populations of the resulting materials are more sensitive to both metal identities and synthetic procedure (e.g. order of reagent addition), suggesting that certain principles of metal chalcogenide post-synthetic modification are excitingly robust, while also revealing new avenues for both mechanistic discovery and structural control.

Introduction

Post-synthetic modification[1-8] strategies are powerful and well-investigated methods for transforming nanoparticles (NPs) into complex, multi-component nanostructures that may not be accessible through direct synthetic pathways. In addition, NPs that consist of multiple phases within a single structure often exhibit dual or synergistic physical and chemical properties and are of growing interest for a wide range of applications including heterogeneous catalysis,[9-12] photovoltaic devices,[13-16] displays,[17-20] biological imaging, and therapeutics.[21-23] In these multicomponent NPs, both the identities of the components and their arrangement within the NP architecture impact the properties of the resulting material.[24, 25]

These structure-property relationships have motivated numerous studies and introduced a wide range of nanoheterostructures (NHSs), ranging from binary architectures with two distinct crystalline phases to complex architectures with as many as 5 distinct crystallographic phases.[4, 24, 26-30] From these studies, common growth modes

[a] *Department of Chemistry, University of Pittsburgh, Pittsburgh, Pennsylvania 15260, United States.*
[b] *McKetta Department of Chemical Engineering, University of Texas at Austin, Austin, Texas 78712, United States*
^ *Department of Chemical and Petroleum Engineering, University of Pittsburgh, Pittsburgh, Pennsylvania 15260, United States.*
+ *Department of Mechanical Engineering and Materials Science, University of Pittsburgh, Pittsburgh, Pennsylvania 15260, United States.*

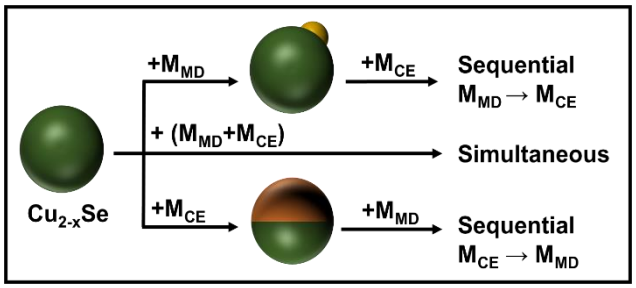

Scheme 1. Schematic representation of the three synthetic approaches of metal cation addition to $Cu_{2-x}Se$ NPs studied here.

and driving forces have emerged. Common modes of post-synthetic nanoparticle growth include cation exchange (CE)[31-33] and metal deposition (MD).[6, 7, 29, 34, 35] The driving forces that dictate the incorporation mode, and the extent of that incorporation, are known to depend on factors such as the reduction potentials of the metal ions, lattice formation energies, lattice volume and symmetry changes[4], metal ion radii,[36] metal ion coordination number[37] and lattice mismatch between the incoming metal and the host particle.[38-42] With these various factors governing the formation of NHSs, it is interesting to study the interactions between these parameters and the influence of those interactions on nanoparticle outcomes, with the goal of identifying progressively more comprehensive synthetic insights, and ultimately achieving systematic design and synthesis of targeted, complex NHSs.

One way to interrogate the relative influence of a given synthetic parameter is to use established binary relationships, and challenge them with a third synthetic component. For example, it is well known that Pb^{2+}, Ag^{+}, Cu^{+}, Cu^{2+}, and Hg^{2+} undergo cation exchange spontaneously with CdS and CdSe in polar solvents, likely because the solubility product (K_{sp}) of the cadmium chalcogenides are higher than the resulting metal chalcogenides.[43, 44] However, in non-polar media, solubility factors can be circumvented in the presence of phosphine facilitators, such as tri-octyl phosphine, where Ag_2S can be converted to CdS, understood via a hard-soft acid base mechanism preferentially coordinating silver cations.[42] These examples highlight the difficulty in identifying general strategies for understanding, and ultimately predicting, NHS outcomes. However, in revealing these discrepancies, there is also an opportunity to refine our conclusions about the conditions under which various synthetic tools may be used for predictive synthesis.

In this report, we investigate the addition of pairs of metal cations, simultaneously and sequentially, to $Cu_{2-x}Se$ NPs (**Scheme 1**). The metal pairs (Ag-Au, Ag-Pt, Hg-Au and Hg-Pt) are chosen such that one metal incorporates via CE and the other via MD when added individually to the $Cu_{2-x}Se$ NPs.[5] Surprisingly, we find that each metal combination, across all three synthetic routes, yield metal-semiconductor hybrids that incorporate metals via both CE and MD without deviation from the outcomes observed for the binary systems.

Results

In a typical experiment, we first synthesized water-dispersible $Cu_{2-x}Se$ NPs with an average diameter of 52 ± 5 nm using a seed-mediated approach.[45] We use $Cu_{2-x}Se$ NPs because they are readily synthesized via an aqueous, benchtop synthesis, their plasmonic properties make them ideal candidates for downstream applications, and they exhibit an isotropic crystal structure, limiting complications arising from different facets that makes studying post-synthetic modification outcomes more straightforward. Having selected an appropriate starting material, we then post synthetically introduced four combinations of two metal salt solutions to the system ($HAuCl_4$ and $AgNO_3$, $HAuCl_4$ and $Hg(NO_3)_2$, K_2PtCl_4 and $AgNO_3$, K_2PtCl_4 and $Hg(NO_3)_2$) and evaluated changes in $Cu_{2-x}Se$ NP composition and morphology.

We considered several variables when selecting the secondary metals to be used in these experiments, as well as in selecting the metal combinations. The individual metals were chosen because their mode of post-synthetic incorporation into $Cu_{2-x}Se$ NPs (and analogous metal chalcogenides) has been relatively well described.[1, 46-49] Metal combinations were chosen such that each pair is comprised of a metal that shows incorporation via metal deposition (MD) (Au and Pt) and cation exchange (CE) (Ag and Hg). The motivation for this combination approach was two-fold: 1) to test the interaction of the metal cations with one another and reveal competitive parameters that may change the outcome of combination from their individual additions

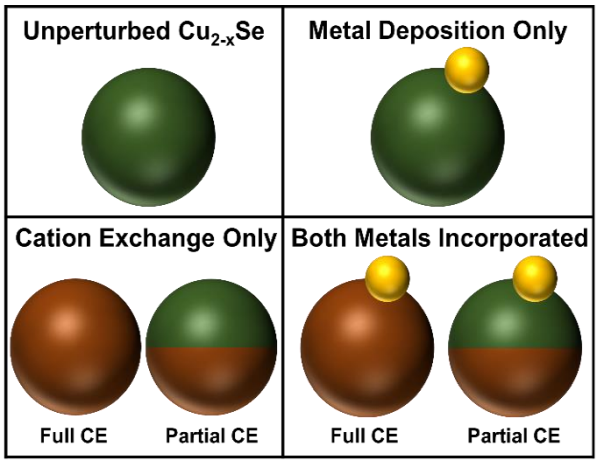

Chart 1. Schematic representation of the products observed for multi-metal addition to $Cu_{2-x}Se$ NPs.

and, 2) to generate heterostructures with both multi-metal chalcogenide phases and metal-semiconductor interfaces.

With these strategically chosen metal cation pairs in hand, we post-synthetically added ascorbic acid to the synthesized and purified $Cu_{2-x}Se$ NPs followed by addition of each of the four metal cation pairs, either simultaneously or sequentially under ambient conditions (see **Experimental Section** in Supporting Information). We then used a variety of techniques to characterize the resulting NHSs, including scanning transmission electron microscopy-energy dispersive X-ray spectroscopy (STEM-EDS) to evaluate the spatial distributions of Cu, Se, and secondary metals, powder X-ray diffraction (PXRD) to probe bulk crystallographic features, and UV–vis-NIR

extinction spectroscopy to monitor resulting optoelectronic properties. Here, we outline the results of these studies, including a statistical analysis of particle products (**Chart 1**). Overall, we observed a remarkable fidelity with bimetallic post-synthetic modification outcomes (i.e. whether metals incorporate via MD or CE). However, we also observe metal combination specific morphology outcomes that reveal considerable tunability in both the form and extent of either MD or CE in the ternary systems. Below, we describe our findings for each metal combination individually, and then summarize the unifying and distinguishing aspects of the syntheses in aggregate.

Silver and Gold Addition. The post-synthetic addition of Au and Ag cations to $Cu_{2-x}Se$ NPs resulted in the incorporation of Ag by CE and Au by MD (as pendant metal islands, **Figure 1 A-C**). For all three synthetic approaches (i.e. simultaneous addition of Ag and Au cations, sequential addition of Ag and Au cations: both Ag first and Au first), Ag was incorporated exclusively through CE and Au exclusively via MD. The PXRD patterns (**Figure 1D**) support the formation of AgSe and CuAgSe phases as well as a metallic Au phase. We do not observe metallic Ag either by XRD or by STEM-EDS. The average diameter of the $Cu_{2-x}Se$ after all three synthesis routes is similar to the original $Cu_{2-x}Se$ NPs (42±7 nm vs. 52±5 nm) (**Figure S13 and Table S1**). The Au domain size in all three synthetic routes were also similar (17±5 nm averaged across all three syntheses). Extinction spectroscopy analysis (**Figure S17A**), shows an expected dampening of the $Cu_{2-x}Se$ localized surface plasmon resonance (LSPR) as reported previously upon cation exchange.[1, 5] In addition, there is no observable LSPR peak that might be associated with either deposited Ag islands or homogeneously nucleated Ag NPs. We do observe a LSPR peak from the Au domain at ~ 620 nm. For the Ag-Au combination, Ag cation exchanges and Au deposits as an island on the top of the $Cu_{2-x}Se$ NP, as expected from the individual addition of the metal cations to $Cu_{2-x}Se$ NPs, with no alloying of the Au deposit. These results suggest that for this particular combination of metals the reaction-insensitive parameter of lattice symmetry distortion[5] remains the dominant driving force that predicts the NHS architecture in this ternary system.

To better understand the synthetic outcomes, we analyzed the distribution of resulting NPs morphologies for all three synthetic approaches (**Figure 2**). In all approaches, over 75% of particles undergo post-synthetic modification: either CE, MD, or both (**Figure 2A**). Across all routes, the percentage of particles that undergo CE only, MD only, and both processes are also similar (approximately a third of the modified population is CE only, MD only, or both) (**Figure 2B**). However, the distribution of CE products (i.e. full vs. partial CE) varies with the synthetic route (**Figure 2C**). After simultaneous addition of Au and Ag cations, for the NPs that incorporate a metal via CE and incorporate both metals via MD and CE, the percentage of partially cation exchanged NPs is significantly larger than that of fully CE NPs (30% vs 1%). On the other hand, when cations were added sequentially, the order of addition impacted the relative populations of full and partial CE outcomes for NPs that underwent both CE and MD (Ag→Au: 1%/30%; Au→Ag:14%/18%). NPs that underwent CE only during sequential addition exhibited a full/partial CE distribution similar to the simultaneous addition case (Ag→Au: 16%/23%; Au→Ag:17%/19%).

Silver and Platinum Addition. Addition of Ag and Pt salt solutions, sequentially and simultaneously, to the $Cu_{2-x}Se$ solution resulted in Ag incorporation via CE and Pt via MD, as dendrites (**Figure 3**). As suggested by STEM-EDS maps and supported by PXRD patterns (**Figure 3D**), each synthesis yields particles with $Cu_{2-x}Se$, AgSe and CuAgSe phases. Interestingly, STEM-EDS maps and corresponding linescans suggest that the pendant islands that form on top of the $Cu_{2-x}Se$ in each of the three methods, has a ternary metallic composition of Pt, Cu and

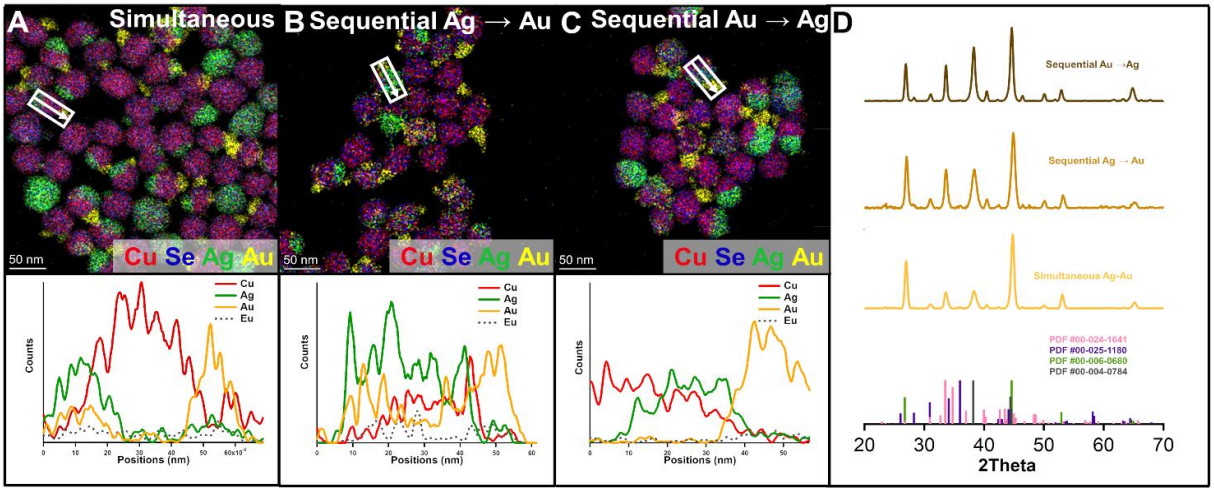

Figure 1. (A-C) Representative STEM-EDS maps and generated linescans of (A) Simultaneous Ag-Au, (B) Sequential Ag → Au (C) Sequential Au → Ag containing composite NPs. Cu Kα, Se Lβ, Ag Lα and Au Lα signals are represented in red, blue, green, and yellow, respectively. White boxes indicate the location used to extract line scan data, with the arrowhead indicating the direction. Dotted gray lines in linescan plots represent Eu signal, which is used as background signal comparison. HAADF and individual elemental maps can be found in the Supporting Information. *N. B.* Any difference in contrast between maps should not be taken as quantitative. (D) PXRD patterns of NPs resulting from simultaneous Ag-Au, sequential Ag → Au and sequential Au → Ag additions. Included PXRD references are $Cu_{2-x}Se$ (PDF # 00–006–0680, green), Ag_2Se (PDF #00–024–1041, pink), CuAgSe (PDF #00–025–1180, purple) and Au (PDF # 00–004 –0784, light gray) and are represented in vertical lines.

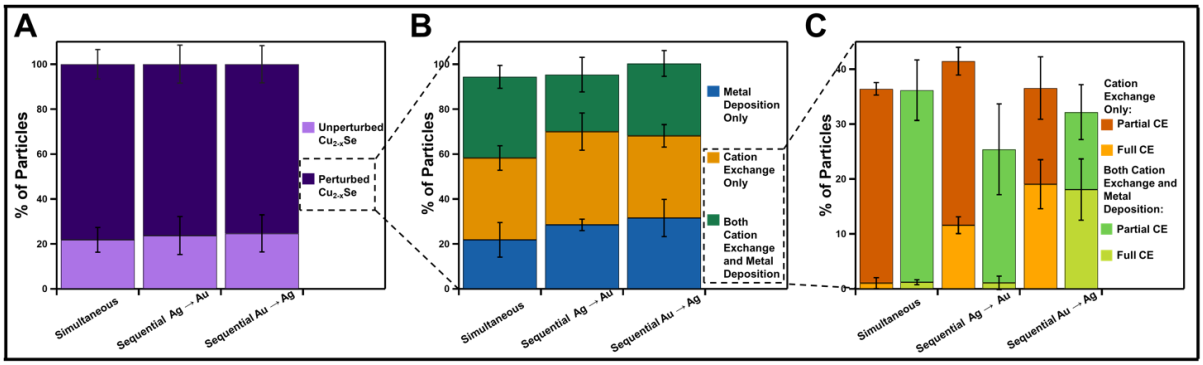

Figure 2: (A) Percentage of NPs either modified ("perturbed," dark purple) or unmodified ("unperturbed," light purple) during the 3 syntheses. (B) Of the modified particle population (dark purple), the percentage of NPs containing only Au (MD only, blue), only Ag (CE only, yellow) and both Ag and Au (both CE and MD, green); (C) of the particles that underwent CE, the percentage of NPs containing only the Ag with partial (yellow) and both Ag and Au metals (green), measured across at least 150 particles and 3 experimental replicates.

Ag, indicating additional redox processes between the $Cu_{2-x}Se$ and incoming metal cations (**Figure 3 A-C** and *vide infra*, Discussion). The $Cu_{2-x}Se$ core size remained unchanged after secondary metal incorporation, and the Pt domain size is consistent across all three synthetic routes (18±5 nm) (**Figure S14 and Table S2**).

The extinction spectra of all three synthetic routes show a dampened $Cu_{2-x}Se$ LSPR, consistent with the incorporation of Ag and Pt in the material (**Figure S17B**). In the case of Ag-Pt addition we still see the Ag incorporation via CE and Pt via MD is observed, consistent with what is observed in the case of their individual addition. However, in the case of the multimetallic

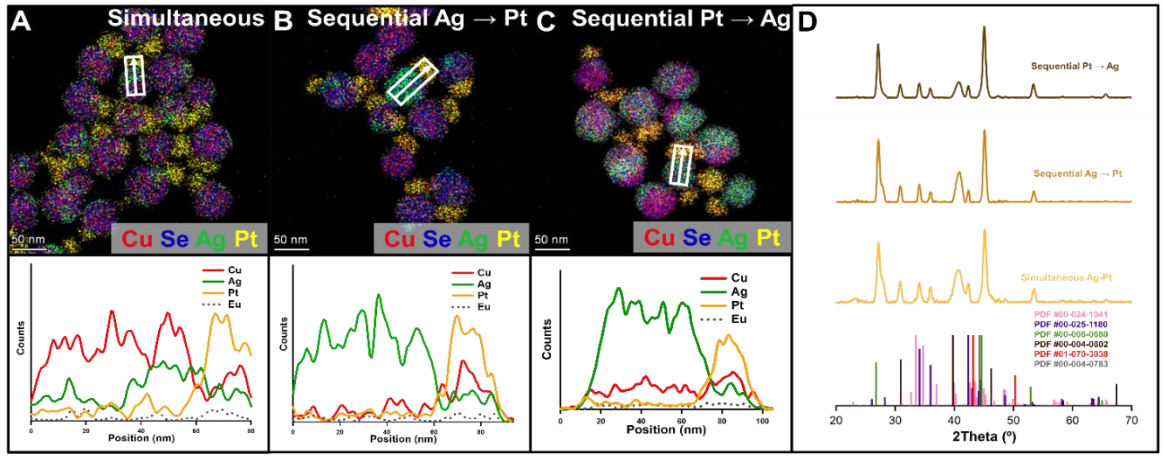

Figure 3. (A-C) Representative STEM-EDS maps and generated linescans of (A) Simultaneous Ag-Pt, (B) Sequential Ag → Pt (C) Sequential Pt → Ag containing composite NPs. Cu Kα, Se Lβ, Ag Lα and Pt Lα signals are represented in red, blue, green, and yellow, respectively. White boxes indicate the location used to extract line scan data, with the arrowhead indicating the direction. Dotted gray lines in line scan plots represent Eu signal, which is used as background signal comparison. HAADF and individual elemental maps can be found in the Supporting Information. *N. B.* Any difference in contrast between maps should not be interpreted as quantitative. (D) PXRD patterns of simultaneous Ag-Pt, sequential Ag → Pt and sequential Pt → Ag. Included PXRD references are $Cu_{2-x}Se$ (PDF # 00–006–0680, green), Ag_2Se (PDF #00–024–1041, pink), CuAgSe (PDF #00–025–1180, purple), Pt (PDF #00–004–0802, dark brown), and Cu (PDF # 01–070–3038, red) and Ag (PDF # 00–004 –0783, light gray) are represented in vertical lines.

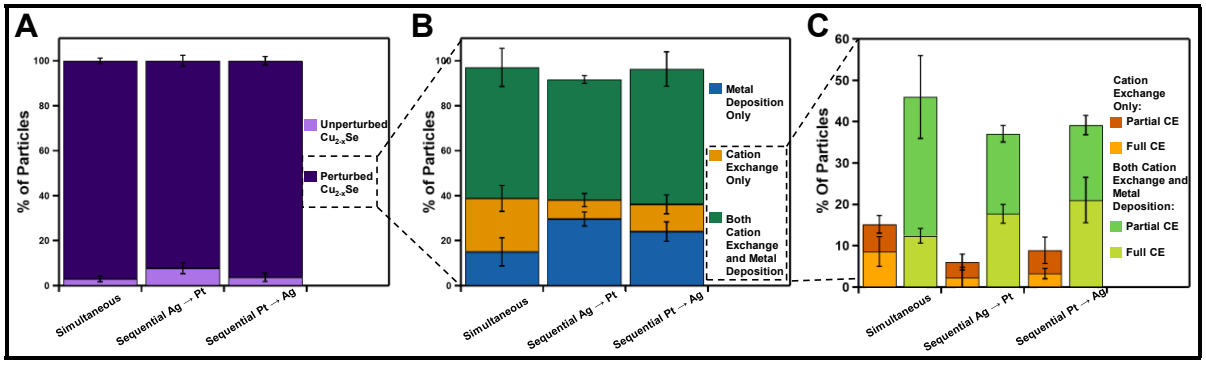

Figure 4. (A) Percentage of NPs either modified ("perturbed," dark purple) or unmodified ("unperturbed," light purple) during the 3 syntheses. (B) Of the modified particle population (dark purple), the percentage of NPs containing only Pt (MD only, blue), only Ag (CE only, yellow) and both Pt and Ag (both CE and MD, green); (C) Of the particles that underwent CE, the percentage of NPs containing only the Ag with partial (yellow) and both Ag and Pt metals (green), measured across at least 150 particles and 3 experimental replicates.

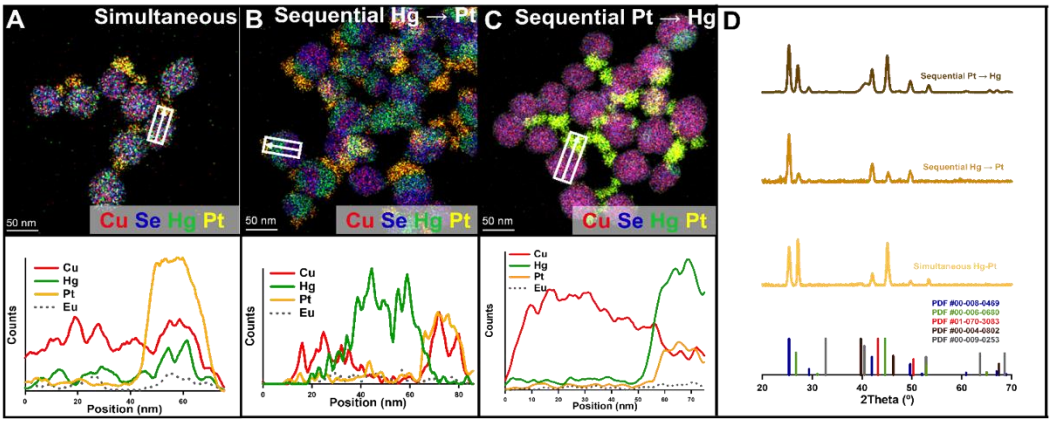

Figure 5. (A-C) Representative STEM-EDS maps and generated linescans of (A) Simultaneous Hg-Pt, (B) Sequential Hg → Pt (C) Sequential Pt → Hg containing composite NPs*. Cu Kα, Se Lβ, Hg Lα and Pt Lα signals are represented in red, blue, green and yellow, respectively. White box indicates the location used to extract line scan data, with the arrow head indicating the direction. Dotted gray lines in linescan plots represent Eu signal, which is used as background signal comparison. *N. B.* Any difference in contrast between maps should not be taken as quantitative. Also, although Hg appears to have a higher concentration in this representative image, we have analyzed other particles and the line scans indicate significant variability in stoichiometry and chemical ordering. (**Figure S21**). (D) PXRD patterns of simultaneous Hg-Pt, sequential Hg → Pt and sequential Pt → Hg. Included PXRD references are $Cu_{2-x}Se$ (PDF # 00–006–0680, green), HgSe (PDF #00–008–0469, blue), Hg (PDF # 00-009-0253, light gray), Pt (PDF #00–004–0802, dark brown), and Cu (PDF # 01–070–3038, red) resented in vertical lines.

addition, regardless of the sequence of addition, the composition of the island becomes complex, consisting of Pt, Cu and Ag. Similar results of PtCu mixing have been observed in previous studies[5, 49]. In this case, the metal chalcogenide host has $Cu_{2-x}Se$, as well as AgSe and CuAgSe phases. Therefore, the formation of a ternary PtCuAg phase on the pendant island is likely because now both Ag and Cu are available for incorporation into the metallic island from the chalcogenide host (*vide infra*).

Mercury and Platinum Addition. Like the combinations of Ag-Au and Ag-Pt, the addition of Hg and Pt salts to the pre-synthesized $Cu_{2-x}Se$ NPs, yields products where Hg cation exchanges with Cu, and Pt adds to the structure via MD. However, unlike the Ag-Au and Ag-Pt, in the case of Hg-Pt the sequence of metal addition influences the specific compositions and morphologies of the MD and CE products. Specifically, in both simultaneous metal ion addition as well as each permutation of sequential addition, we observe incorporation of Hg into the lattice via CE, and the deposition of dendritic Pt islands on the $Cu_{2-x}Se$ (**Figure 5**), however the composition of the resulting metal islands varies. In the sequential addition of Hg then Pt, the metal island formed on the $Cu_{2-x}Se$ NP contains only Pt and Cu (**Figure 5B**). However, upon the simultaneous addition and the sequential permutation of Pt first, the island has a ternary metal composition of Cu, Pt and Hg (**Figure 5 A, C**). The extinction spectra of NPs resulting from each synthetic route show similar trends with a dampened and red-shifted $Cu_{2-x}Se$ plasmon as a result of Hg and Pt incorporation (**Figure S17C**). The $Cu_{2-x}Se$ core size remains unchanged after secondary metal incorporation, and the Pt domain size is consistent across all three synthetic routes (17±5 nm) (**Figure S15 and Table S3**).

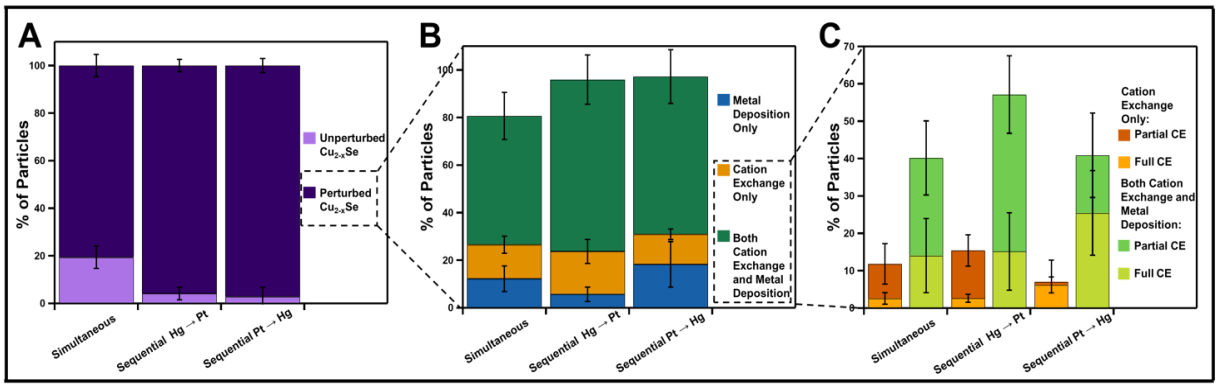

Figure 6. (A) Percentage of NPs either modified ("perturbed," dark purple) or unmodified ("unperturbed," light purple) during the 3 syntheses. (B) Of the modified particle population (dark purple), the percentage of NPs containing only Pt (MD only, blue), only Hg (CE only, yellow) and both Pt and Hg (both CE and MD, green); (C) of the particles that underwent CE, the percentage of NPs containing only the Hg with partial (yellow) and both Hg and Pt metals (green), measured across at least 150 particles and 3 experimental replicates.

All three synthetic approaches show more than 80% conversion of $Cu_{2-x}Se$ NPs to incorporate one or both metals either via CE, MD or both (**Figure 4A**). Also, across all three synthetic routes, the percentage of particles that incorporated both metals (i.e. underwent both CE and MD) were more than those that incorporated one metal by either CE or MD only (Both: 60% vs. CE only or MD only: <30%) (**Figure 4B**). For all three approaches, particles that underwent CE (including particles that showed CE only and particles that showed both CE and MD), showed more partially cation exchanged particles than fully cation exchanged particles (**Figure 4C**).

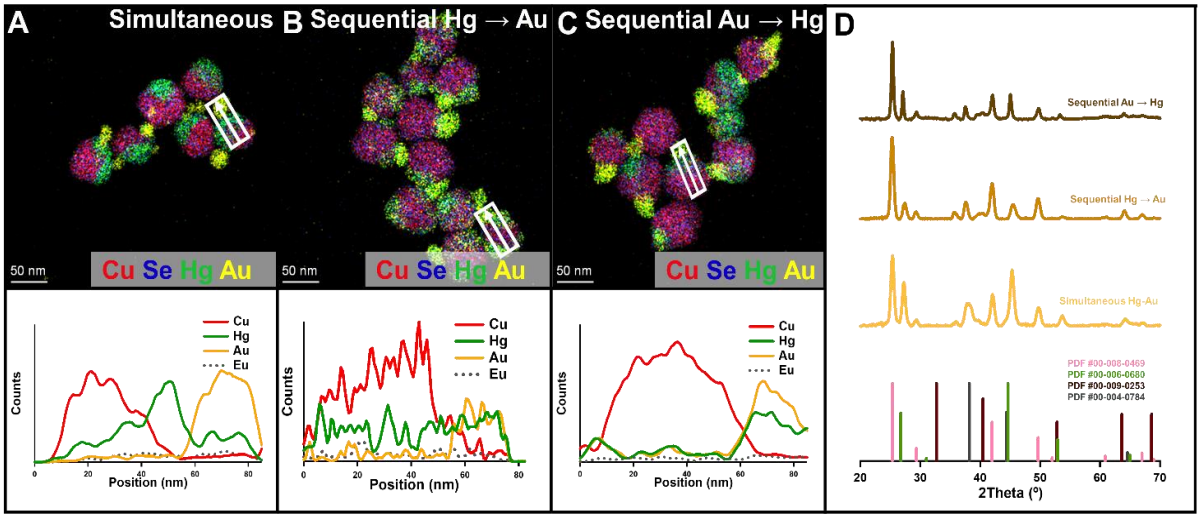

Figure 8. (A-C) Representative STEM-EDS maps and generated linescans of (A) Simultaneous Hg-Au, (B) Sequential Hg → Au (C) Sequential Au → Hg containing composite NPs. Cu Kα, Se Lβ, Hg Lα and Au Lα signals are represented in red, blue, green and yellow, respectively. White box indicates the location used to extract line scan data, with the arrow head indicating the direction. Dotted gray lines in linescan plots represent Eu signal, which is used as background signal comparison. HAADF and individual elemental maps can be found in the Supporting Information. *N. B.* Any difference in contrast between maps should not be interpreted as quantitative. (D) PXRD patterns of simultaneous Hg-Au, sequential Hg → Au and sequential Au → Hg. Included PXRD references are $Cu_{2-x}Se$ (PDF # 00–006–0680, green), HgSe (PDF #00–008–0469, pink), Hg (PDF #00-009-0253, dark brown), and Au (PDF # 00–004 –0784, light gray) are represented in vertical lines.

Overall, statistical analysis of STEM-EDS results indicates that more than 80% of particles undergo post-synthetic modification (either CE, MD or both) (**Figure 6A**). Of these particles, the majority incorporate both metals across all three synthetic approaches (Both: >41% vs. CE or MD only: <18%) (**Figure 6B**). Hg-Pt, the metal islands in the Hg-Au case are alloys for all three synthesis routes (**Figures 7**). However, unlike the cases of Ag-Pt and Hg-Pt, no Cu is present in the alloy deposit. The extinction spectra (**Figure S17D**) show a dampening of the $Cu_{2-x}Se$ plasmon which is consistent with Hg CE, and a Au peak at ~620 nm due

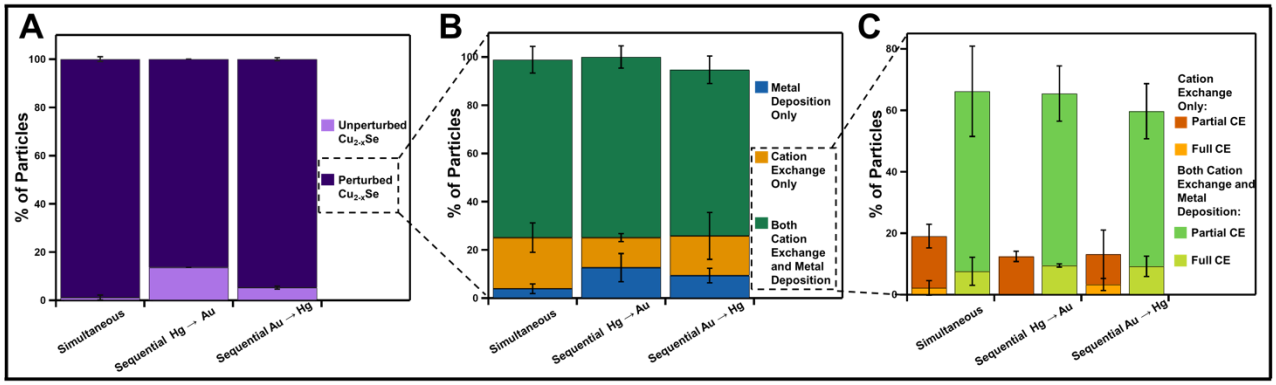

Figure 7. (A) Percentage of NPs either modified ("perturbed," dark purple) or unmodified ("unperturbed," light purple) during the 3 syntheses. (B) Of the modified particle population (dark purple), the percentage of NPs containing only Au (MD only, blue), only Hg (CE only, yellow) and both Hg and Au (both CE and MD, green); (C) of the particles that underwent CE, the percentage of NPs containing only the Hg with partial (yellow) and both Hg and Au metals (green), measured across at least 150 particles and 3 experimental replicates.

Of those particles that show CE only, for simultaneous and sequential Hg→Pt addition, the percentage of particles that show a partial CE morphology is higher than those that show full CE (12% vs. 2%). Whereas for sequential Hg→Pt addition, particles that show CE only, show equal amounts of partial and full CE (~6%) (**Figure 6C**). However, for particles that incorporate both metals, for all three synthetic approaches, the majority of the population exhibits partial CE over full CE (>40% vs. <25%).

Mercury and Gold Addition. Hg and Au addition show incorporation of Hg into the $Cu_{2-x}Se$ lattice by CE and deposition of Au island on top of the NPs, for all three synthetic routes by PXRD and STEM-EDS. However, as with the cases of Ag-Pt and to the Au domain deposition. The size of $Cu_{2-x}Se$ core is also preserved after secondary metal incorporation, with relatively monodisperse metal deposition domains (20±6 nm, **Figure S16 and Table S4**).

Similar to the three other metal combinations previously discussed, the mode of Hg and Au incorporation does not change in these synthetic approaches, showing no deviation from the binary system. But for this metal combination, similar to the Ag-Pt and Hg-Pt additions (*vide supra*), the composition and stoichiometry of the resulting metal islands are complex.

Similar to the other three metal combinations, all three synthetic approaches show more than 80% of the $Cu_{2-x}Se$ NPs undergo post-synthetic modification (**Figure 8A**). Across all

three synthetic routes, the majority of these particles incorporate both metals showing CE and MD both (Both: >70%, vs. CE or MD only: <21%) (**Figure 8B**). The CE morphology distribution is also consistent across all cases, with more partial CE vs. full CE for both particles that show CE only and those which incorporate both (Both: >60%/<10%; CE only: >13%/<3%) (**Figure 8C**).

Discussion

Taken together, for all four metal combinations investigated, the mode of individual metal incorporation does not deviate from the mode observed during individual metal cation addition (*i.e.* if the metal undergoes CE in the binary system, we observed that it also underwent CE in the ternary systems we tested, and this similarity with binary synthesis outcomes was also true for metals that favour MD). While these overarching outcomes are encouraging for the generality of post-synthetic modification strategies for the $Cu_{2-x}Se$ NP class, detailed analysis of the morphological outcomes reveal important points of heterogeneity for further study including 1) varying population of particles that undergo CE/MD only vs. those that undergo both, 2) extent of CE (full CE vs. partial CE), 3) composition of CE domains, and 4) composition of metal deposited domains.

First, examining NP populations that incorporate at least one secondary metal (**Figure S19**), these may be particles that have undergone either MD or CE only, or particles that have undergone both. Here, each synthesis route yields approximately the same percentage of morphologies for the same metal combination. However, heterogeneity arises when comparing results between the metal combinations. For the Au-Ag combination, the percentage of NPs that incorporate both metals (~27-35%) is significantly lower than what is observed for the other metal combinations (>65%). The lower ternary content of the Au-Ag combination indicates that in the case of Au-Ag addition, Ag CE and Au deposition may interfere with one another. One explanation for this outcome may be the higher lattice mismatch between Au and Ag_2Se and CuAgSe (~35-47%) than between Au and $Cu_{2-x}Se$ (28%). Another explanation could be, that the deposition of Au pendant island on the $Cu_{2-x}Se$ surface leads to a less accessible surface for the Ag ions to diffuse into the lattice, but given the partial coverage of the Au deposits, this explanation seems less likely (**Tables S5** and **S6**).

Next, we consider the variation in the extent of CE (e.g. partial vs. full CE) observed for each metal combination. With the exception of sequential Au→Ag addition, across all metal combinations and across each synthetic route within a specific combination (i.e. for both NPs that show CE only and those that show both CE and MD), the percentage of NHSs exhibiting partial cation exchange is more than those undergoing full cation exchange (<30% of the particles across all particle outcomes exhibit full CE, **Figure S20**). This distribution is an indication that CE under these circumstances does not follow a co-operative mechanism.[50, 51] If a cooperative mechanism was followed, one would expect to observe a higher population of fully cation exchanged NPs, as the incorporation of the incoming metal ions into a NP would cause more of the secondary metal to infiltrate that same particle until either there is no more secondary metal left to incorporate or the particle is completely transformed. There is one exception in our metal combinations: the case of sequential Au→Ag addition. Here, the extent of CE in terms of relative populations of fully vs. partially cation exchanged particles is more even, showing slightly higher full CE (54±5% vs. 46±8% respectively). This result is consistent with a previous study of silver CE, where silver CE follows a cooperative mechanism.[1]

Similar to our results regarding the relative populations of fully vs. partially cation exchanged NPs, heterogeneity in the composition of the CE domains agrees well with previous studies of binary systems. For example, for Ag-Au and Ag-Pt combinations, we observe the formation of both Ag_2Se and CuAgSe phases. Whereas, with Hg-Au and Hg-Pt, only HgSe phase is formed. These results agree with what has been observed for individual additions of Hg and Ag ions to $Cu_{2-x}Se$ under similar conditions: Ag_2Se, CuAgSe, and HgSe form readily while CuHgSe is not observed likely due to its monoclinic crystal structure which represents a large symmetry deviation from the cubic $Cu_{2-x}Se$ and thus likely an unfavourable transformation.[5]

Finally, we consider the heterogeneity in composition of the deposited metal islands. By analysing the varying alloy compositions, we can suggest a series of hypotheses concerning the chemical driving forces leading to the multimetallic islands. In the case of multimetallic islands containing Pt, the Pt dendrites that deposit on the $Cu_{2-x}Se$ NP have an increased surface area compared to a non-dendritic Pt-island of similar volume.[52, 53] One explanation for island alloying is that unpassivated sites on the Pt dendrite surfaces could serve as preferential reduction sites for solubilized Cu, Hg, and Ag (from the chalcogenide host) in combination with ascorbic acid which is also in solution and can act as a reducing agent.

However, this explanation is not sufficient for at least one of the cases studied here. In the case of Hg→Pt, HgSe is formed and then Pt ions are added to yield metal island deposits containing only Pt and Cu. Hg is not present in the islands in this case. For this metal combination and synthesis route, we examine parameters that could influence the composition of the metal islands, including lattice symmetry, bond dissociation enthalpy (BDE) and solubility product of the possible metal selenides (**Table S7**). The K_{sp} of HgSe is much lower than $Cu_{2-x}Se$, which means that once HgSe forms, dissolution into Hg^+ ions are more unfavourable than the formation of $Cu^{+/2+}$ from $Cu_{2-x}Se$. Given this difference in solubility, it is less likely that there are either remaining *or* leached Hg^+ ions in solution when Pt deposits. In contrast to the case of simultaneous Pt-Hg and sequential Pt → Hg addition, where there are Hg cations in solution that can be incorporated into the island to form the PtCuHg ternary metal composite islands observed here.

Conclusions

We have reported a small library of ternary metal-semiconductor hybrid heterostructures using aqueous, air-stable $Cu_{2-x}Se$ NPs as the starting material. These structures are

studied and obtained using both the simultaneous and sequential addition of four metal combinations. Taken together, the results suggest that pathways of CE or MD in post-synthetic modification of $Cu_{2-x}Se$ are preserved when challenged with the addition of a second metal or with varying synthetic procedures. However, several axes of heterogeneity are present within those broader CE or MD outcomes, yet are still relatively well explained by known mechanistic parameters. Overall, we view the results of this synthetic study and the resulting new structures as encouraging support for the broader applicability of synthetic insights gained here and elsewhere in the synthesis of metal-metal chalcogenide nanoheterostructures.

Author Contributions

The manuscript was written through contributions of all authors. All authors have given approval to the final version of the manuscript.

Conflicts of interest

There are no conflicts to declare.

Acknowledgements

This work was supported by the Defense Threat Reduction Agency (Grant No HDTRA1-21-1-0019). R.S acknowledges previous support from University of Pittsburgh Mary E. Warga Fellowship. T.M.G. acknowledges previous support from University of Pittsburgh Wass Summer Undergraduate Fellowship. S.L.M. acknowledges previous support from Summer Research Fellowship from the University of Pittsburgh. J.H.S. acknowledges previous support from A&S Fellowship from the University of Pittsburgh.

Notes and references

1. E. A. Eikey, X. Y. Gan, D. C. Kaseman, C. G. E. Murphey, S. E. Crawford, K. A. Johnston, S. Yazdi and J. E. Millstone, *Chemistry of Materials*, 2020, **32**, 1322-1331.
2. L. F. Garcia-Herrera, H. P. McAllister, H. Xiong, H. Wang, R. W. Lord, S. K. O'Boyle, A. Imamovic, B. C. Steimle, R. E. Schaak and K. E. Plass, *Chem. Mater.*, 2021, **33**, 3841-3850.
3. B. J. Beberwyck, Y. Surendranath and A. P. Alivisatos, *The Journal of Physical Chemistry C*, 2013, **117**, 19759-19770.
4. A. G. Butterfield, L. T. Alameda and R. E. Schaak, *Journal of the American Chemical Society*, 2021, **143**, 1779-1783.
5. X. Y. Gan, R. Sen and J. E. Millstone, *Journal of the American Chemical Society*, 2021, **143**, 8137-8144.
6. N. Diemler, *Journal*, 2019.
7. P. J. Straney, N. A. Diemler, A. M. Smith, Z. E. Eddinger, M. S. Gilliam and J. E. Millstone, *Langmuir*, 2018, **34**, 1084-1091.
8. M. J. Enright and B. M. Cossairt, *Chemical Communications*, 2018, **54**, 7109-7122.
9. P. Balaya, *Energy & Environmental Science*, 2008, **1**, 645-654.
10. D. B. Miracle and O. N. Senkov, *Acta Materialia*, 2017, **122**, 448-511.
11. C. Coughlan, M. Ibáñez, O. Dobrozhan, A. Singh, A. Cabot and K. M. Ryan, *Chemical Reviews*, 2017, **117**, 5865-6109.
12. M. D. Regulacio and M.-Y. Han, *Accounts of Chemical Research*, 2016, **49**, 511-519.
13. H. A. Atwater and A. Polman, *Nature Materials*, 2010, **9**, 205-213.
14. M. K. L. Man, A. Margiolakis, S. Deckoff-Jones, T. Harada, E. L. Wong, M. B. M. Krishna, J. Madéo, A. Winchester, S. Lei, R. Vajtai, P. M. Ajayan and K. M. Dani, *Nature Nanotechnology*, 2017, **12**, 36-40.
15. Y. Zhan, Z. Shao, T. Jiang, J. Ye, X. Wu, B. Zhang, K. Ding, D. Wu and J. Jie, *Journal of Materials Chemistry A*, 2020, **8**, 789-796.
16. Y. Zhou, H. Zhao, D. Ma and F. Rosei, *Chemical Society Reviews*, 2018, **47**, 5866-5890.
17. N. Oh, B. H. Kim, S.-Y. Cho, S. Nam, S. P. Rogers, Y. Jiang, J. C. Flanagan, Y. Zhai, J.-H. Kim, J. Lee, Y. Yu, Y. K. Cho, G. Hur, J. Zhang, P. Trefonas, J. A. Rogers and M. Shim, *Science*, 2017, **355**, 616-619.
18. Y. Shirasaki, G. J. Supran, M. G. Bawendi and V. Bulović, *Nature Photonics*, 2013, **7**, 13-23.
19. X.-g. Wu, H. Ji, X. Yan and H. Zhong, *Nature Nanotechnology*, 2022, **17**, 813-816.
20. A. Castelli, B. Dhanabalan, A. Polovitsyn, V. Caligiuri, F. Di Stasio, A. Scarpellini, R. Brescia, M. Palei, B. Martín-García, M. Prato, L. Manna, I. Moreels, R. Krahne and M. P. Arciniegas, *Advanced Optical Materials*, 2020, **8**, 1901463.
21. Kenry, Y. Duan and B. Liu, *Advanced Materials*, 2018, **30**, 1802394.
22. W. Song, P. Jia, T. Zhang, K. Dou, L. Liu, Y. Ren, F. Liu, J. Xue, M. S. Hasanin, H. Qi and Q. Zhou, *Journal of Nanobiotechnology*, 2022, **20**, 289.
23. H. Huang, W. Feng, Y. Chen and J. Shi, *Nano Today*, 2020, **35**, 100972.
24. C. Steimle Benjamin, L. Fenton Julie and E. Schaak Raymond, *Science*, 2020, **367**, 418-424.
25. L. Manna, J. Cheon and R. E. Schaak, *Accounts of Chemical Research*, 2021, **54**, 1543-1544.
26. J. T. Mulder, N. Kirkwood, L. De Trizio, C. Li, S. Bals, L. Manna and A. J. Houtepen, *ACS Applied Nano Materials*, 2020, **3**, 3859-3867.
27. I. Rosina, B. Martín-García, D. Spirito, Z. Dang, G. Gariano, S. Marras, M. Prato, R. Krahne, L. De Trizio and L. Manna, *Chemistry of Materials*, 2020, **32**, 2978-2985.

28. L. Najafi, S. Bellani, A. Castelli, M. P. Arciniegas, R. Brescia, R. Oropesa-Nuñez, B. Martín-García, M. Serri, F. Drago, L. Manna and F. Bonaccorso, *Chemistry of Materials*, 2020, **32**, 2420-2429.
29. L. Huang, B. Shen, H. Lin, J. Shen, L. Jibril, C. Y. Zheng, C. Wolverton and C. A. Mirkin, *Journal of the American Chemical Society*, 2022, **144**, 4792-4798.
30. N. Kirkwood, A. De Backer, T. Altantzis, N. Winckelmans, A. Longo, F. V. Antolinez, F. T. Rabouw, L. De Trizio, J. J. Geuchies, J. T. Mulder, N. Renaud, S. Bals, L. Manna and A. J. Houtepen, *Chemistry of Materials*, 2020, **32**, 557-565.
31. C. R. McCormick and R. E. Schaak, *Journal of the American Chemical Society*, 2021, **143**, 1017-1023.
32. R. E. Schaak, B. C. Steimle and J. L. Fenton, *Accounts of Chemical Research*, 2020, **53**, 2558-2568.
33. Y. Sun, K. Fujisawa, Z. Lin, Y. Lei, J. S. Mondschein, M. Terrones and R. E. Schaak, *Journal of the American Chemical Society*, 2017, **139**, 11096-11105.
34. A. M. Fagan, W. R. Jeffries, K. L. Knappenberger, Jr. and R. E. Schaak, *ACS Nano*, 2021, **15**, 1378-1387.
35. R. W. Lord, C. F. Holder, J. L. Fenton and R. E. Schaak, *Chemistry of Materials*, 2019, **31**, 4605-4613.
36. L. De Trizio, H. Li, A. Casu, A. Genovese, A. Sathya, G. C. Messina and L. Manna, *Journal of the American Chemical Society*, 2014, **136**, 16277-16284.
37. R. Tu, Y. Xie, G. Bertoni, A. Lak, R. Gaspari, A. Rapallo, A. Cavalli, L. De Trizio and L. Manna, *Journal of the American Chemical Society*, 2016, **138**, 7082-7090.
38. L. De Trizio and L. Manna, *Chemical Reviews*, 2016, **116**, 10852-10887.
39. J. Liu and J. Zhang, *Chemical Reviews*, 2020, **120**, 2123-2170.
40. B. C. Steimle, R. W. Lord and R. E. Schaak, *Journal of the American Chemical Society*, 2020, **142**, 13345-13349.
41. C. G. Sharp, A. D. P. Leach and J. E. Macdonald, *Nano Letters*, 2020, **20**, 8556-8562.
42. J. Gui, M. Ji, J. Liu, M. Xu, J. Zhang and H. Zhu, *Angewandte Chemie International Edition*, 2015, **54**, 3683-3687.
43. H. Qu, L. Cao, G. Su, W. Liu, R. Gao, C. Xia and J. Qin, *Journal of Nanoparticle Research*, 2014, **16**.
44. X. Yang, H. Xue, J. Xu, X. Huang, J. Zhang, Y. B. Tang, T. W. Ng, H. L. Kwong, X. M. Meng and C. S. Lee, *ACS Appl Mater Interfaces*, 2014, **6**, 9078-9084.
45. X. Y. Gan, S. E. Crawford, E. A. Eikey, R. Sen, J. R. Killinger and J. E. Millstone, *The Journal of Physical Chemistry C*, 2020, **124**, 4747-4754.
46. M. A. H. Muhammed, M. Döblinger and J. Rodríguez-Fernández, *Journal of the American Chemical Society*, 2015, **137**, 11666-11677.
47. X. Liu, X. Wang and M. T. Swihart, *Chemistry of Materials*, 2013, **25**, 4402-4408.
48. C. Dabard, J. Planelles, H. Po, E. Izquierdo, L. Makke, C. Gréboval, N. Moghaddam, A. Khalili, T. H. Dang, A. Chu, S. Pierini, C. Abadie, M. Cavallo, E. Bossavit, X. Z. Xu, P. Hollander, M. Silly, E. Lhuillier, J. I. Climente and S. Ithurria, *Chemistry of Materials*, 2021, **33**, 9252-9261.
49. A. Wolf, D. Hinrichs, J. Sann, J. F. Miethe, N. C. Bigall and D. Dorfs, *The Journal of Physical Chemistry C*, 2016, **120**, 21925-21931.
50. A. L. Routzahn and P. K. Jain, *Nano Letters*, 2014, **14**, 987-992.
51. S. L. White, J. G. Smith, M. Behl and P. K. Jain, *Nature Communications*, 2013, **4**, 2933.
52. X. Sun, K. Jiang, N. Zhang, S. Guo and X. Huang, *ACS Nano*, 2015, **9**, 7634-7640.
53. X. Du, S. Luo, H. Du, M. Tang, X. Huang and P. K. Shen, *Journal of Materials Chemistry A*, 2016, **4**, 1579-1585.